

# Investigation of flexural properties and failure behaviour of biaxial braided CFRP

Yuan, H., Cai, R., Meng, Q. & Wang, L.

Author post-print (accepted) deposited by Coventry University's Repository

**Original citation & hyperlink:**

Yuan, H, Cai, R, Meng, Q & Wang, L 2020, 'Investigation of flexural properties and failure behaviour of biaxial braided CFRP', *Polymer Testing*, vol. 87, 106545.

<https://dx.doi.org/10.1016/j.polymertesting.2020.106545>

DOI 10.1016/j.polymertesting.2020.106545

ISSN 0142-9418

Publisher: Elsevier

**NOTICE: this is the author's version of a work that was accepted for publication in *Polymer Testing*. Changes resulting from the publishing process, such as peer review, editing, corrections, structural formatting, and other quality control mechanisms may not be reflected in this document. Changes may have been made to this work since it was submitted for publication. A definitive version was subsequently published in *Polymer Testing*, 87, (2020) DOI: 10.1016/j.polymertesting.2020.106545**

© 2020, Elsevier. Licensed under the Creative Commons Attribution-NonCommercial-NoDerivatives 4.0 International <http://creativecommons.org/licenses/by-nc-nd/4.0/>

Copyright © and Moral Rights are retained by the author(s) and/ or other copyright owners. A copy can be downloaded for personal non-commercial research or study, without prior permission or charge. This item cannot be reproduced or quoted extensively from without first obtaining permission in writing from the copyright holder(s). The content must not be changed in any way or sold commercially in any format or medium without the formal permission of the copyright holders.

This document is the author's post-print version, incorporating any revisions agreed during the peer-review process. Some differences between the published version and this version may remain and you are advised to consult the published version if you wish to cite from it.

# Investigation of flexural properties and failure behaviour of biaxial braided CFRP

Hao Yuan <sup>a</sup>, Rui Cai <sup>b\*, c</sup>, Qingshi Meng <sup>d</sup>, Lin Wang <sup>b, c</sup>

<sup>a</sup> Department of Aeronautics, Imperial College London, SW7 2AZ, UK

<sup>b</sup> School of Mechanical, Aerospace and Automotive Engineering, Coventry University, Coventry, CV1 5FB, UK

<sup>c</sup> Institute for Future Transport and Cities, Coventry University, Coventry, CV1 5FB, UK

<sup>d</sup> College of Aerospace Engineering, Shenyang Aerospace University (SAU), Shenyang, 110136, China

\*Corresponding Author: Rui Cai

Email: rui.cai@coventry.ac.uk

**Key words:** Biaxial braided CFRP; fibre volume fraction (FVF); three-point bending; finite element analysis (FEA)

## Abstract

In this research, the experimental tests of quasi-static three-point bending and three-point bending fatigue were carried out for a  $\pm 25^\circ$  biaxial braided carbon fibre reinforced polymer (CFRP) manufactured using vacuum assisted resin transfer moulding (VARTM). A finite element (FE) model was also set up for quasi-static testing and the *prediction results revealed that local fibre volume fraction (FVF) is a primary source affecting the mechanical properties of braided CFRP*. The fatigue of the braided CFRP was defined as three different stages according to the flexural modulus results. The damage modes of the test specimens were observed via *a* digital microscope and scanning electron microscope (SEM) and the process-induced defects were summarised. With compiled results and observations, this study provides a better understanding of failure and fatigue behaviour of biaxial braided composites and their flexural properties *which offers* a good basis for any further research in fibre volume fractions, structure design and manufacturing for braided CFRP.

## 1. Introduction:

The increasing application of composite materials in multiple disciplines, such as aerospace, civil engineering and rapidly growing automotive industry, has raised the need for the development of manufacturing processes to improve the cost-efficiency, material throughput and product quality in the mass production [1–4]. Braiding is one of the most cost-effective and versatile textile production processes as the fibre preforms have a variety of producible textile characteristics and *also* allow the near net-shaped preforms to be produced for hollow and slender structures [5,6]. The net-shape braided composite tube structures have superior performance to those tubes made of overlapped stitched fabric reinforcements [7]. However, Arold et al. summarised that the fibre undulation and waviness of biaxial braided composites lead to some shortcomings of biaxial braids in high performance applications [5]. The failure mechanisms and fatigue damages for braided fabric are complicated. For braids under tension, the kink bands could be provoked by the off-axis shear stress in undulated fibre sections [8] while the discontinuous reinforcements *could cause* local stress concentrations [9]. The delamination and formation of kink band are the main reasons for micro buckling [10,11].

The fibre volume fraction is one of the key factors for determining both mechanical and physical properties of composite materials, and it is an important part of *the* statistical characterisation of composite microstructure [12]. High fibre volume fractions are favourable for the mechanical characteristics of composite materials, and the fibre volume fractions are approximately 60% for typical carbon fibre reinforced polymer (CFRP) composites [13]. Uniaxial CFRP composites with fibre volume fraction as high as 90% with *the* potential of ultimate mechanical properties were successfully produced via bi-dimensional compression moulding proposed by Ashbee [14]. McCarthy and Vaughan reported that *only a little difference was found between the transverse* failure surfaces for composites with 40% and 59% volume fractions, but the transverse strength is much higher for 20% volume fraction due to the greater inter-fibre spacing (however, this would decrease the longitudinal strength) [15]. *In a transverse fibre bundle test, Qi et al. found that the decrease of local fibre volume content can increase the carbon fibre/matrix bonding strength* [16]. Jensen observed the significant inhomogeneity of elastic strain in static and creep testing on normally flat UD composites [17]. Variations of laminated thickness and fibre volume fraction were suggested as two potential causes.

Apart from fibre volume fraction, woven fabrics braiding patterns (e.g. diamond, regular, Hercules), and especially desired braiding angle on the braiding technique also play important roles in affecting its mechanical properties [18]. The study of failure and damage characterisation of a  $\pm 30^\circ$  biaxial braided composites under multiaxial stress states has been carried out by Cichosz et al. using off-axis oriented specimens [6]. Zhao et al. proposed two methods (equivalent

1D material method and equivalent laminate method) that can predict the moduli and strengths of braided composites with fibre angle ranging from  $15^\circ$  to  $75^\circ$  [19]. In Kelkar and Whitcomb's experiment, the braids were slit to reduce the variation of braiding angle caused by flattening of the braids [20]. The edge condition of the braids could have effects on strength: 100% increase of strength for ( $\pm 15^\circ$ ) braid [21] and 13% increase for ( $\pm 45^\circ$ ) braid compared to coupons with edges cut open [22]. Tate et al. reported the sensitivity of the tensile properties to braid angle and the drop was found in the tensile strength, modulus and Poisson's ratio as the braid angle increased from  $25^\circ$  to  $45^\circ$  [23]. Tate and Kelkar developed a methodology in further research for prediction of fatigue life and residual fatigue modulus via employing sigmoidal function and Bradley function [24].

Meanwhile, finite element (FE) analysis *was* applied for meso and microstructure level investigation braided composites failure and factors which affect their mechanical properties such as fibre volume fractions and the manufacture techniques. Wu et al. developed a microstructure level FE model with a volume fraction of 25.45% for investigation on the bending fatigue properties of a 3D braided composite [25]. The authors reported that *there are stress concentrations in the contact area between yarns and resin* and debonding was caused by the difference of loading in matrix and yarns. Hao et al. investigated the fatigue behaviour of 3D four directional braided composites with various braiding angles and fibre volume fractions using a unit cell model under tension-tension loading at different directions [26]. The fibre volume fraction was adjusted via changing the diameter of the fibre yarns. Jensen et al. built a finite element (FE) model for different samples using transversely isotropic composite material properties for different fibre volume fractions [27]. Mühlstädt et al. investigated the intra-yarn fibre volume fraction gradients in the laminated plain-woven fabrics based on the meso-level and micro-level structure and proposed a mathematical model to describe the intra-yarn fibre volume fraction gradients [28]. Wehrkamp-Richter et al. developed a 3D novel meso-level unit cell modelling approach with compaction effects from manufacturing for prediction of the non-linear mechanical properties of a triaxial braided composite [29]. Faes et al. proposed a 2D modelling method based on high-resolution microscopic images to predict the crack initiation within the nested textile composite *considering inhomogeneity of intra-yarn fibre volume fractions* [30]. To date, both experimental studies and numerical modelling are mainly focused on 3D braids but only *a* few experimental studies mechanical properties of biaxial braided composites. In this research, a biaxial braided carbon fibre composite structure was manufactured using the low-cost vacuum assisted resin transfer moulding (VARTM). The detailed VARTM process was explained by Tate et al. [31] and the thickness and fibre volume fraction control for VARTM was introduced in [32, 33]. Due to the inevitable manipulation of the raw materials during *the* manufacturing processes, the braided composite parts will always have the local variation of fibre angle and *uneven resin distribution*

to different extend. The low coverage of the biaxial braids on the mandrel can also result in an increased fibre undulation, thus, a decreased mechanical performance [34]. Due to the various limitations of existing modelling methods, the effects of the process-induced imperfections cannot be taken into account at the same time [30]. Both FE model and failure mechanism observations can be adopted to assist the research. The aim of the current study is to provide the damage and failure characterisation of a  $\pm 25^\circ$  biaxial CFRP under both static and fatigue three-point loadings via the observations from a digital microscope and scanning electron microscope (SEM). *This study also investigated the relationship between the failure and fibre volume fractions with the support of stress-strain results from the tests and FE models, and hence provide the guidance for manufacture techniques.*

## 2. Experimental Section

### 2.1 Materials

The rectangular braided CFRP tubular material in this study is shown in Figure 1 (a). The preform was produced by over-wrapping each of two non-structural closed cell cross-linked polyethylene foam blocks with a biaxial carbon braid sleeve and then over-wrapping the two wrapped foam blocks together with a larger biaxial carbon braid sleeve. *The preform then was injected with Crestapol® 1260 urethane acrylate resin. The overall fibre volume fractions of these components recorded by the manufacturer are mainly between 40% to 50%. The braided composite laminate is indicated as blue (inner braids) and purple (outer braid) coloured area as shown in Figure 1 (b). The braided sleeve has a nominal fibre angle of  $25^\circ$  at this component's dimension.*

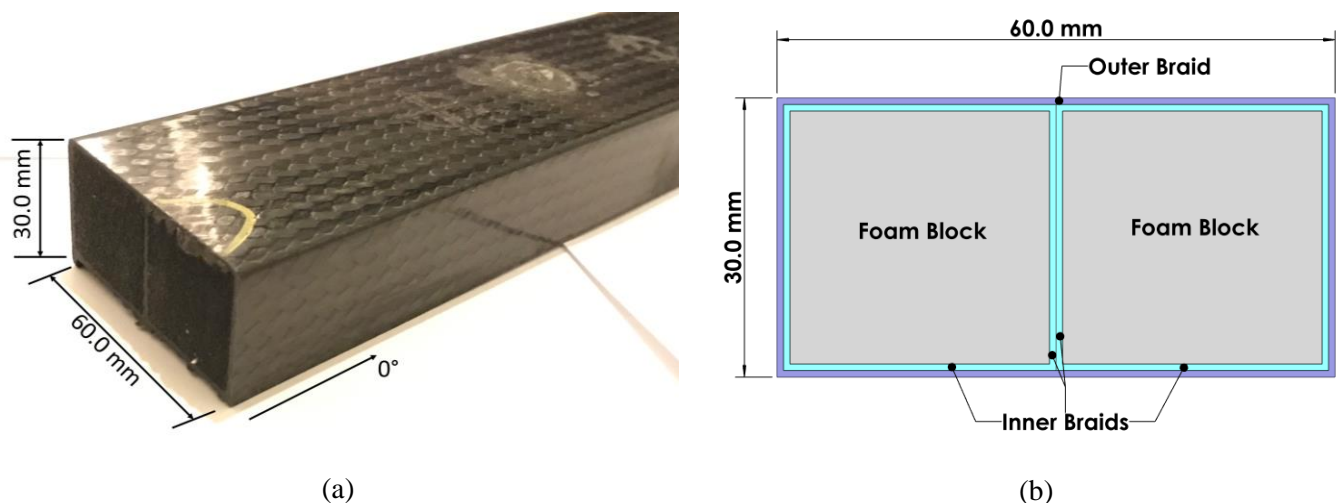


Figure 1 (a) Biaxial braided CFRP component, (b) A schematic sketch of the cross section of the braided CFRP structure

## 2.2 Material properties

The fibre yarns used to braid the carbon sleeve are TORAYCA® T700s 12K carbon fibres and the properties of the fibre and matrix are given in Table 1 [35,36]. Narrow strips were cut from the skin of the finished braided CFRP structure to the dimensions of 150 mm by 25 mm. The excessive foam on the back surface of the coupons was removed.

Table 1 Properties for T700 carbon fibre and cured urethane acrylate resin [35,36]

TORAYCA® T700s		Pure cured resin	
Tensile strength [MPa]	4,900	Tensile strength [MPa]	67
Tensile modulus [MPa]	230,000	Tensile modulus [MPa]	3,500
Strain	2.1%	Strain	2.4%
Density [g/cm <sup>3</sup> ]	1.80	Density [g/cm <sup>3</sup> ]	1.041
Filament diameter [μm]	7	Glass transition temperature [°C]	130

*As the carbon braid which wraps on it have a consistent fibre angle ( $\pm 25^\circ$ ), it can be deduced that there are same amount of fibres in every section within the same area when the raw braided fibres are well-flattened during the manufacturing process.* The local fibre volume fraction at the middle of the specimen where the thickness measurement was taken is calculated using *the* following process.

Figure 2 gives a sketch of the fibre yarn layout in a layer of braid in a specimen (each line represents a fibre yarn). One lamina in a specimen contains 33 warps and 33 wefts (66 yarns) on average and the total length of yarns within a specimen is approximately 5915.5 mm. The volume of the fibres ( $V_f$ ) can be calculated using the properties of TORAYCA® T700s 12K carbon fibres *in Table 1*:

$$V_f = \text{Number of filaments} \times \text{total length of yarns} \times \text{cross section area of the filament} = 12000 \times 5915.5 \text{ mm} \times (\pi \cdot 0.0035^2) \text{ mm}^2 = 2731.9 \text{ mm}^3 \quad (1)$$

The volume of a coupon ( $V_c$ ) can be calculated as:

$$V_c = 150 \text{ mm} \times 25 \text{ mm} \times \text{thickness (mm)} \quad (2)$$

The fibre volume fractions calculated for each test specimen are given in Table 2.

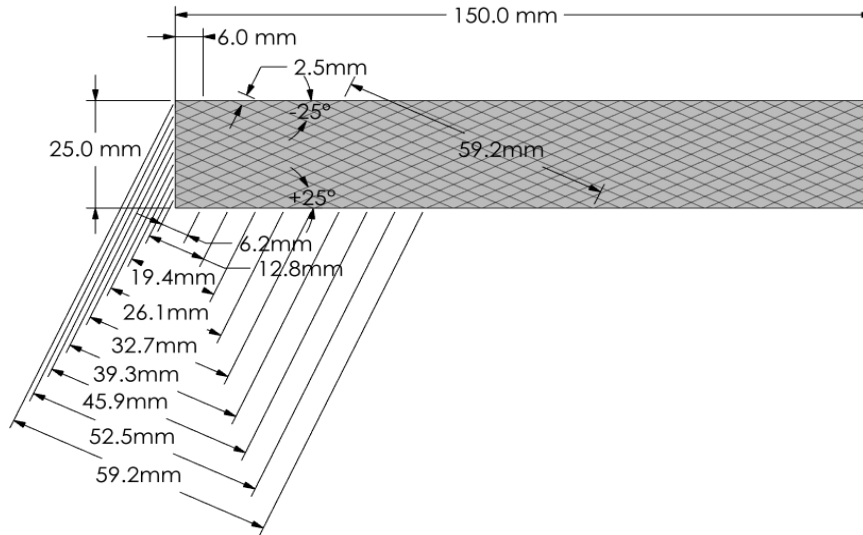


Figure 2 A representation of the layout of fibre yarns in a layer of carbon braid

Table 2 Calculated fibre volume fractions and quasi-static three-point bending test results

Coupon No.	Thickness [mm]	FVF	Flexural modulus [MPa]	Flexural strength [MPa]	Failure strain
S01	2.240	32.51%	11947.0	266.5	2.37%
S02	1.710	42.59%	16796.5	428.0	2.64%
S03	1.692	43.04%	17006.7	383.2	2.39%
S04	1.663	43.78%	16419.5	309.1	1.95%
S05	1.533	47.52%	17712.8	379.4	2.21%
S06	1.416	51.43%	23047.2	387.5	1.76%
S07	1.258	57.91%	30313.4	452.7	1.60%
Average	1.645	45.54%	19034.7	372.3	2.13%
$S_{n-1}$	0.287	7.36%	5933.7	64.7	0.37%

## 2.3 Mechanical tests

### 2.3.1 Quasi-static three-point bending tests

The apparatus and testing procedure followed the ASTM standard D790 [37]. The quasi-static three-point bending tests were carried out on the INSTRON® 5kN static 3-point flexure fixture mounted on the base of the INSTRON® 3369 Universal Testing System. As the apparent modulus of elasticity for highly anisotropic composites can be severely reduced by shear deflections when the laminates are tested at low span-to-depth ratio [38], a span-to-depth ratio of 60:1 (84 mm span) was used. The strain rate was 0.01 mm/mm/min.

### 2.3.2 Three-point bending fatigue tests

The bending fatigue tests were performed on INSTRON® 8871 Servo hydraulic Fatigue Testing System with the same setup as in quasi-static tests. The support span of 84 mm was used. The framework of the fatigue life proposed by Talreja suggested to plot the strain at the vertical axis in place of the stress as in a conventional S-N diagram [39]. Therefore,

the tests were conducted at the laboratory ambient temperature under a displacement-controlled regime, with a testing frequency of 5 Hz. The mean displacement and the amplitude were set to 5.8 mm and 4 mm, respectively, according to the results from static tests.

## 2.4 Experimental results

### 2.4.1 Quasi-static three-point bending test results

The load and deflection history during the quasi-static three-point bending test for each specimen was recorded. The flexural stress ( $\sigma_f$ ) and strain ( $\epsilon_f$ ) during the testing, which are the maximum stress and strain occurred at the midpoint of the outer surface of the specimens, were calculated according to methods in ASTM D790-17 [37]. The thickness used for calculation was measured at the midpoint of each specimen. Flexural strength ( $\sigma_{fM}$ ) is defined as the maximum flexural stress the coupons sustained during each bending test. Figure 3 depicts the stress-strain curves for each test specimen and *the relevant results are also presented in Table 2*. The results give large variations in flexural properties although all coupons behaved very similar under quasi-static bending. The flexural modulus and flexural strength considerably vary among different coupons as a result of the variation of local fibre volume fractions.

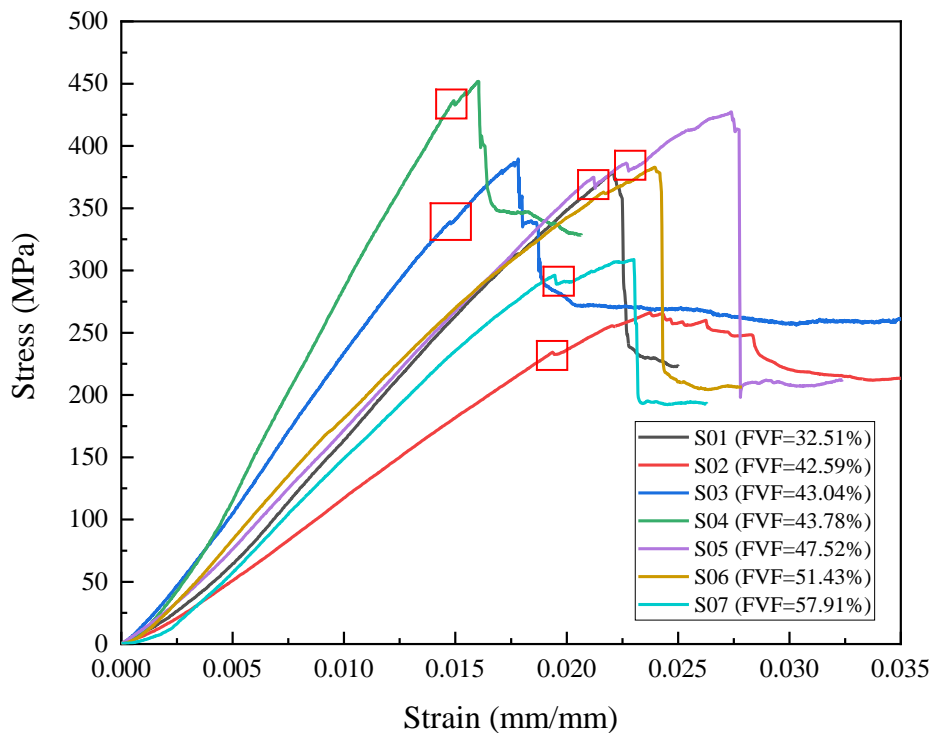


Figure 3 Stress and strain in outer fibres at the midpoint of each specimen

The stress-strain curves show that there were plastic deformation/micro-damages developed before the failure as *the curves started becoming rough following a small drop* as highlighted in Figure 3. This phenomenon was accompanied by the cracking noise emitted from the samples. The material response then entered a very short non-linear region where

one or more drops can be found on the curves and continuous noise occurred as damage developed. The complete failure then occurred, indicated as a sudden large drop on the curves.

#### **2.4.2 Three-point bending fatigue test results**

The stress-strain curves at selected cycles during fatigue tests for four braided CFRP coupons are plotted as hysteresis loops in Figure 4. Each loop represents the maximum stress and strain in the specimen during one cycle of loading and unloading. The accumulated damage energy is represented by the area of each hysteresis loops.

Two scenarios could be found *among four test specimens*. For coupons F01 and F02, the hysteresis loops are closely stick together even at a large increase of number of cycles (e.g. 30000th, 40000th and 54000th cycles for F01) and there is no obvious increase for area of hysteresis loops as the number of cycles grows. The damage energy for these two coupons stopped accumulating when it reached a certain level. Most of the damage energy was able to dissipate during the unloading process within each cycle. Meanwhile, there was no noticeable cracking noise emitted during the whole fatigue process. For coupons F03 and F04, the gaps between hysteresis loops increase as the number of fatigue cycles grows showing the large drop of flexural stiffness, such as the big drops for the hysteresis loops between 1880th and 3180th cycle for coupon F03 and hysteresis loops between 300th and 1120th cycles for coupon F04. The damage energy accumulated at each cycle was not able to fully dissipate during unloading process and the damages from previous cycles were further developed, indicated by *a* larger area of hysteresis loops at these cycles. Specimens, F03 and F04 were failed at this stage as the maximum stress decreases significantly when a constant strain level was applied. Continuous cracking noise was noticed during this stage for both coupons.

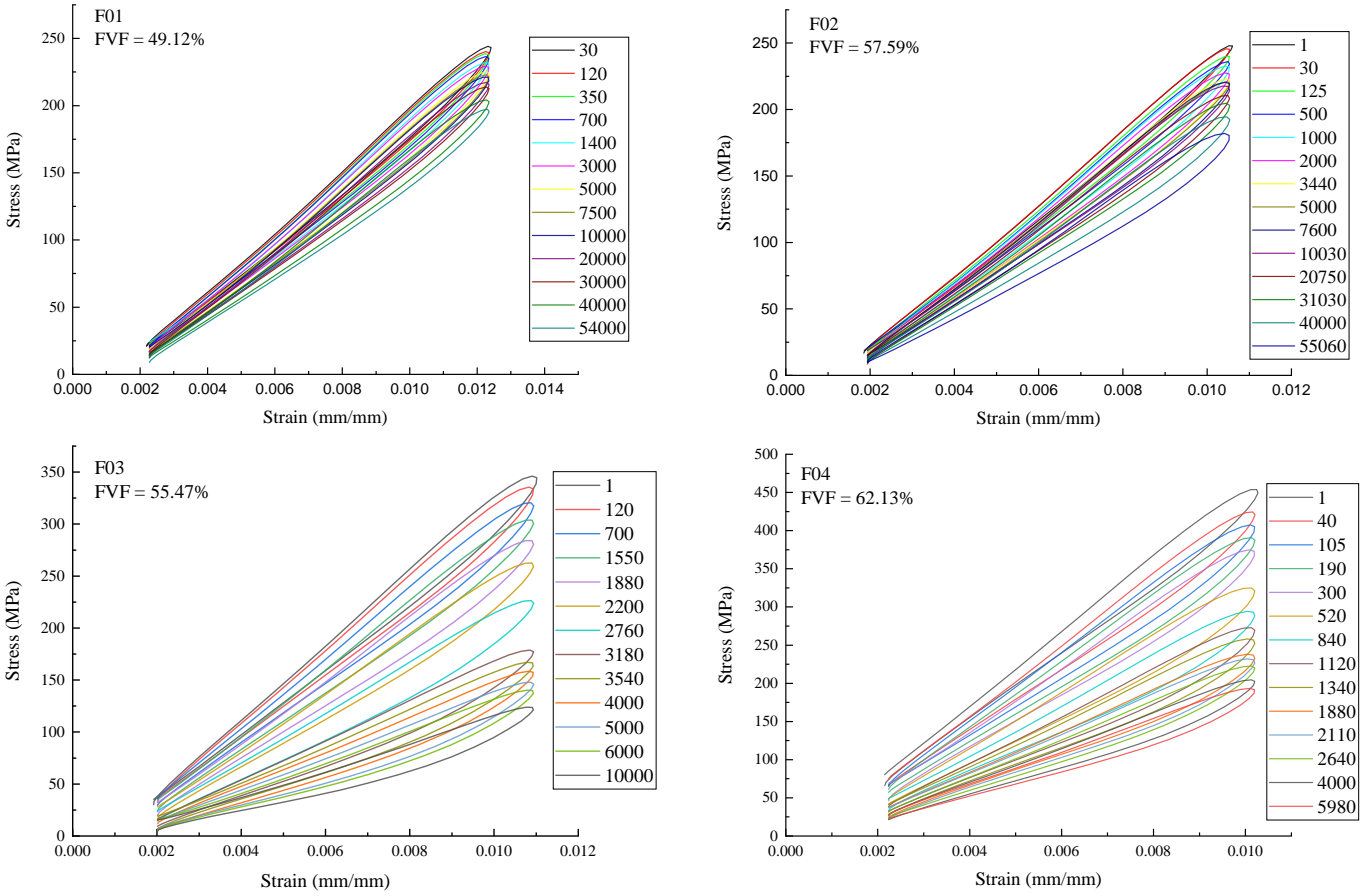


Figure 4 Stress-strain curves for coupon F01, F02, F03 and F04

The relationships between the residual flexural strength and the number of fatigue cycles for above four test specimens are given in Figure 5. The residual flexural modulus percentage ( $M$ ) was defined by Equation (3).

$$M = (E_N/E_1) \times 100\% \quad (3)$$

where  $E_N$  (MPa) is the flexural modulus calculated at a selected cycle during the fatigue testing and  $E_1$  (MPa) is the flexural modulus calculated at the first cycle of bending fatigue. The range of  $M$  is  $[0, 1]$ .

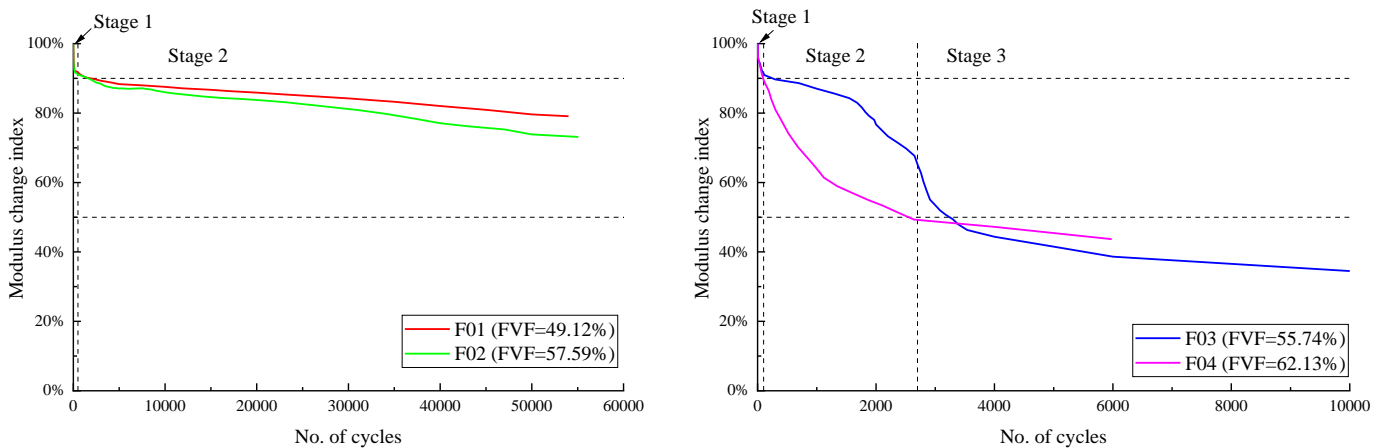


Figure 5 Flexural modulus degradation curves for four different test specimens

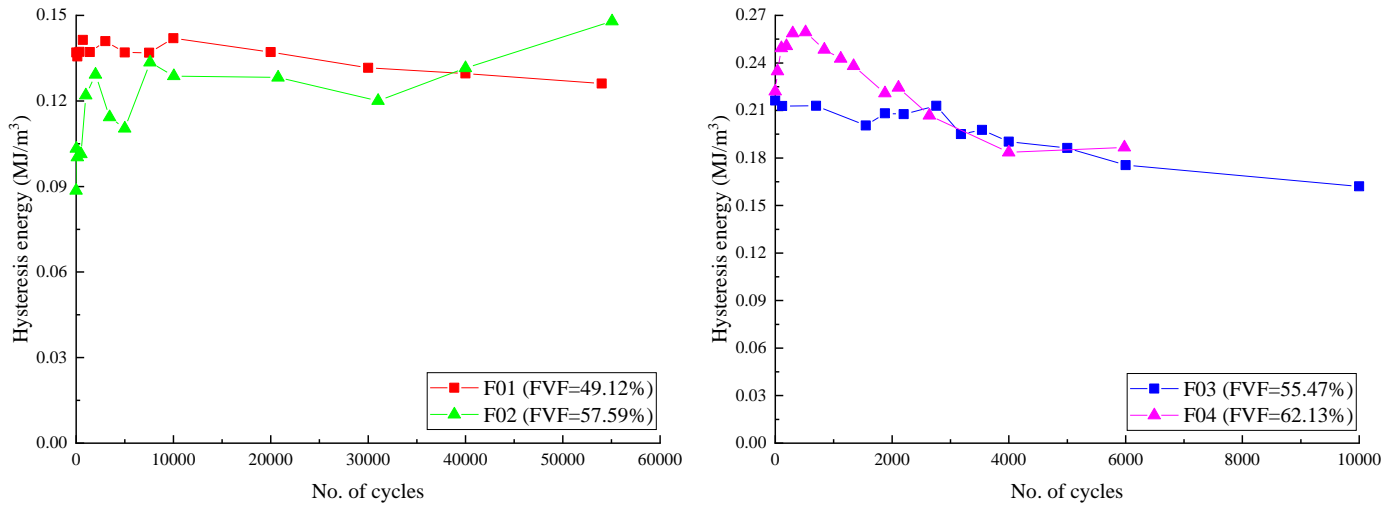


Figure 6 Hysteresis energy history for four different test specimens

Figure 5 shows that the flexural stiffness of all four coupons decreases severely by approximately 10% at the beginning of the fatigue testing and Figure 6 depicts the hysteresis energy absorption during cyclic loading for four specimens.

The stiffness degradation for coupon F01 and F02 then followed a similar pattern decreasing from about 90% residual stiffness to 80% and 74% respectively over 50,000 bending fatigue cycles and the rate of degradation was relatively slow. Although coupon F03 entered this similar status of slowly degraded stiffness after the 10% initial drop, the rate of flexural modulus degradation started increasing at around 1500th cycles and increased again at about 2700th cycles, leading to the failure. The residual stiffness decreased from about 85% to less than 50% through this destructive stage and the degradation rate then started slowing down and became stable again. Coupon F03 and F04 also showed a higher level of hysteresis energy absorption from the start of fatigue testing followed by the stabilisation while Coupons F01 and F02 presented a more stable trend over more than 50,000 loading cycles. For Coupon F04, the flexural modulus dropped rapidly from the beginning of the testing and the failure stage started from the first load cycle and the rate of stiffness degradation reduced with decreased modulus. These phenomena correlate well with the hysteresis loops discussed previously as a significant increase of energy absorption per cycle was observed at the start of the testing.

The fatigue failure process for braided CFRP follows three stages identified above. The first stage is a very short or almost instant process of a sudden drop of the stiffness (10% in this study). The second stage is represented by a relatively long period of slow degradation of the stiffness. If the energy absorbed in each load application is relatively low (0.12-0.15 MJ/m³ for Coupons F01 and F02), the material response tends to be stabilised and may not develop into a complete failure. The third or final stage is the sudden increase in stiffness degradation rate, reducing the stiffness of the composites to a very low level (less than 50% in this study). This happened when hysteresis energy loss is at a higher level as indicated in Coupons F03 and F04 (0.21-0.25 MJ/m³).

### 3. Finite element analysis

#### 3.1 Static three-point bending for test specimens

The upper and lower anvils and coupon were modelled in the commercially available finite element analysis (FEA) software Siemens Femap with NX Nastran (Version 12.0.0). The test specimen was modelled using *plane laminate elements (ANSYS SHELL181) with the composite ply properties in Table 3 provided by the manufacturer. An element size of 2.5 mm was used based on mesh convergence study. Both upper and lower anvils were modelled using linear hexahedron solid elements (ANSYS SOLID185) with properties of tempered 4130 alloy steel. The connectors between anvils and specimen are defined as linear contact and a friction coefficient of 0.25 was used according to Mens and de Gee's study on the friction behaviour between steel and polymers [40]. The analysis was performed for five different laminate thicknesses (1.2 mm, 1.4 mm, 1.6 mm, 1.8 mm and 2 mm) at fibre volume fractions of 40% and 50% separately and for five loads at 20 N intervals (20N, 40N, 60N, etc.). The lamina strength criteria Tsai-Wu theory [41] was applied to the laminate plate elements for failure prediction. Figure 7 shows the examples of the results for z-translation (deflection) and laminate maximum failure index based on Tsai-Wu theory for a test specimen with 1.4 mm thickness and 50% fibre volume fraction under a 120 N load.*

Table 3 Elastic properties of 0° composite plies at fibre volume fraction of 40% and 50%

FVF	E <sub>1</sub> [MPa]	E <sub>2</sub> [MPa]	G <sub>12</sub> [MPa]	G <sub>1z</sub> [MPa]	G <sub>2z</sub> [MPa]	Nu	ρ [g/cm <sup>3</sup> ]
40%	70,476	6,014	2,594	2,029	2,594	0.296	1.3458
50%	87,480	7,800	3,245	2,311	3,245	0.280	1.4215

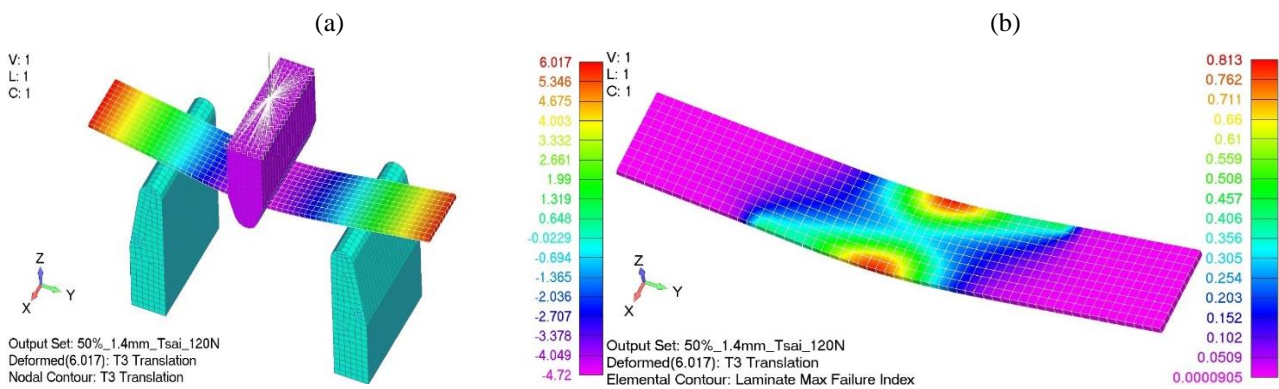


Figure 7 (a) FEA results of z-translation, (b) FEA results of laminate maximum failure index (thickness = 1.4 mm, fibre volume fraction = 50%, load = 120 N)

The results of stress-strain from FEA are plotted in Figure 8 (a). Compared to the experimental results, FEA gave an overestimated stiffness. The strain and stress results were then plotted against maximum laminate failure index according to Tsai-Wu theory as shown in Figure 8 (b) and (c). Two major curves for 40% and 50% fibre volume fractions are presented in each graph in Figure 8. The quadratic curves were used to predict the flexural strength ( $\sigma_{fM}$ ) and failure

strain ( $\epsilon_{fM}$ ) for two volume fractions using the stress and strain at failure index of 1. Less failure strain was found for specimens with higher fibre volume fractions in FEA, following the same trend as in *the* experiments.

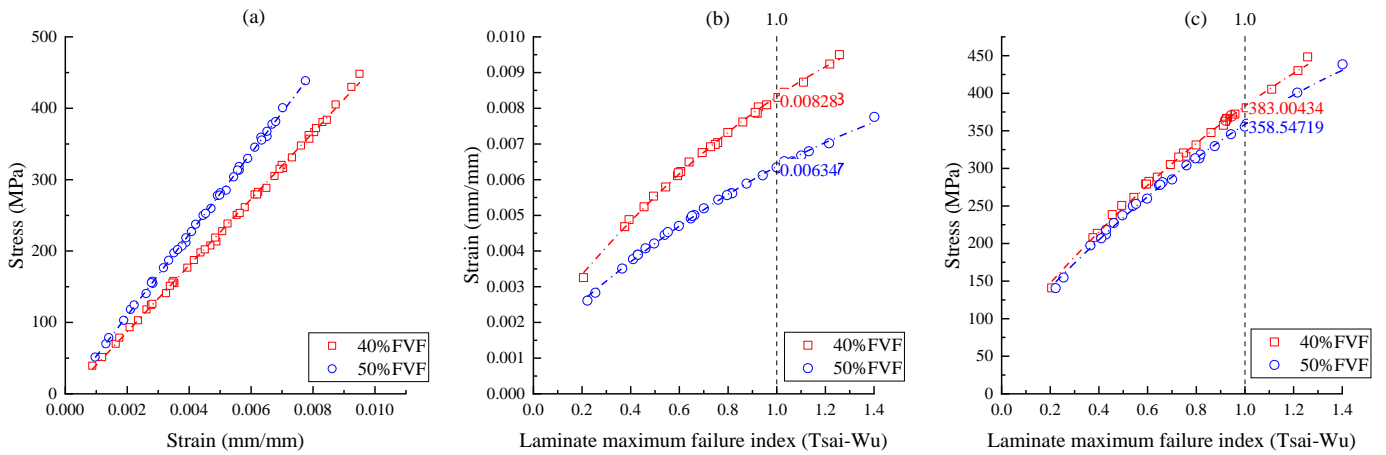


Figure 8 (a) Stress-strain results from FEA, (b) Stress-maximum laminate failure index results from FEA, (c) Strain-maximum laminate failure index results from FEA

The flexural strength and the load at failure derived from Tsai-Wu failure criterion, combined with experimental results, are plotted against the thickness as shown in Figure 9 (a) and Figure 9 (b) respectively. There are only 3 sets of experimental results that fall closely to the region between the two trend lines predicted by FEA. For the load at failure, most of the experimental results closely match the FEA results apart from the coupon with 32.51% fibre volume fraction.

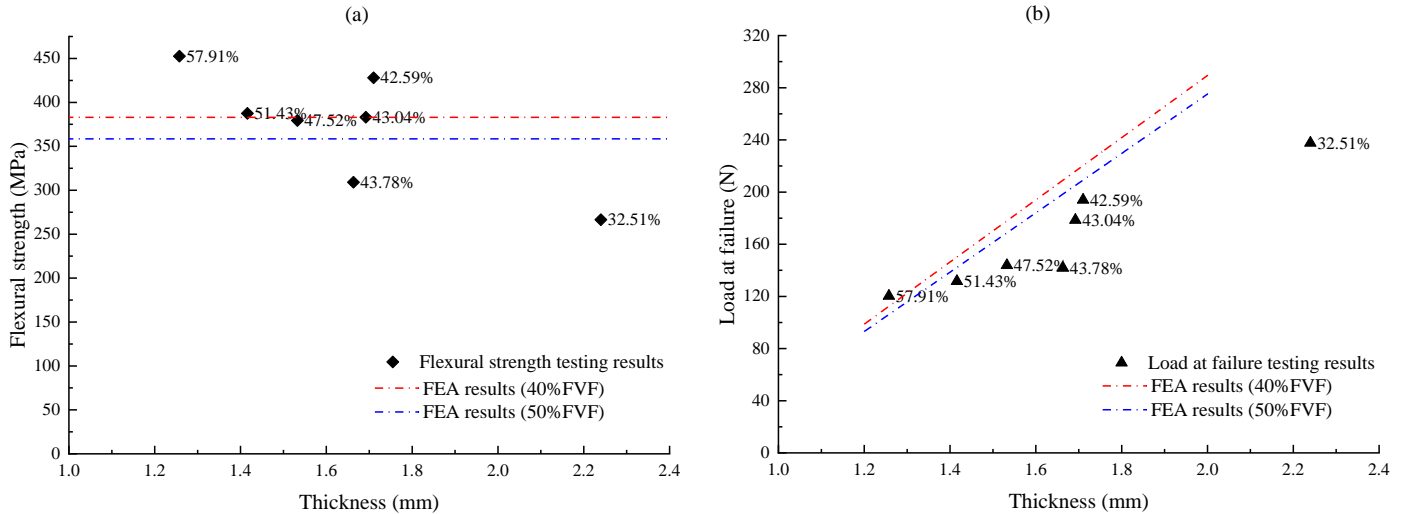


Figure 9 (a) Flexural strength-thickness results from FEA and experiment, (b) Failure load-thickness results from FEA and experiment

### 3.2 Investigation at component level

A whole component described previously *in Figure 1(a)* was tested under the three-point bending load *to investigate the effects of FVF and braid angle on structure performance*. The length of the component in the x-direction is 420 mm and the support span is 350 mm. DBBSM S-Beam load cell and LVDT displacement transducer were used for recording the

force applied and displacement at the centre of the top surface. Three non-destructive tests were performed before a final destructive test.

An FE model was set up *using the same element formulation* as used for simulating the coupon. For this specific component, the average thickness of the outer skins and the middle web are 1.25 mm and 1.60 mm respectively. The element size is set to 5 mm based on mesh convergence study. Linear contact with a friction coefficient of 0.25 was used for the contact regions. The example results of the Z-translation and laminate maximum failure index based on Tsai-Wu criterion at 5254 N load are depicted in Figure 10 (a) and Figure 10 (b). Different magnitudes of the load were applied and the experimental and FEA results are shown in Figure 11 (a).

Tsai-Wu criterion used in FEA *provides a conservative prediction of the structural strength* as the maximum failure index was 1.171 ( $>1$ ) at the failure load of 5254 N. The results of maximum laminate failure index at different load levels were used to predict the failure load by second order polynomial interpolation (4802.1 N as shown in Figure 11 (b)). The location has the most tendencies of failure occurred at the middle of two longitudinal edges on the top surface. The stiffness of the component predicted by the FE model was well correlated to experimental results (around 1393 N/mm) within a large load range (up to about 3700 N) (Figure 11 (a)) before local damages occurred within the component.

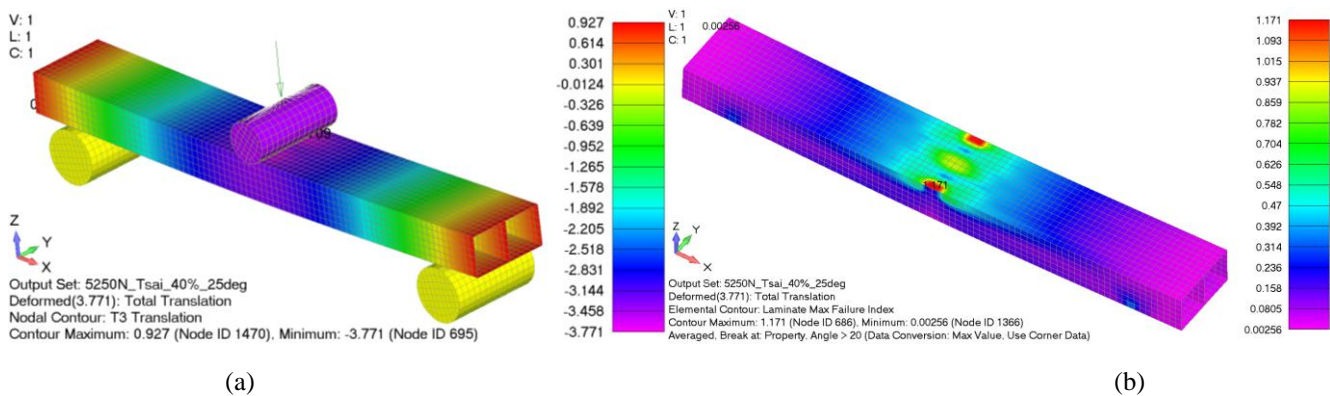


Figure 10 (a) Z-translation results from FEA, (b) Laminate maximum failure index results from FEA

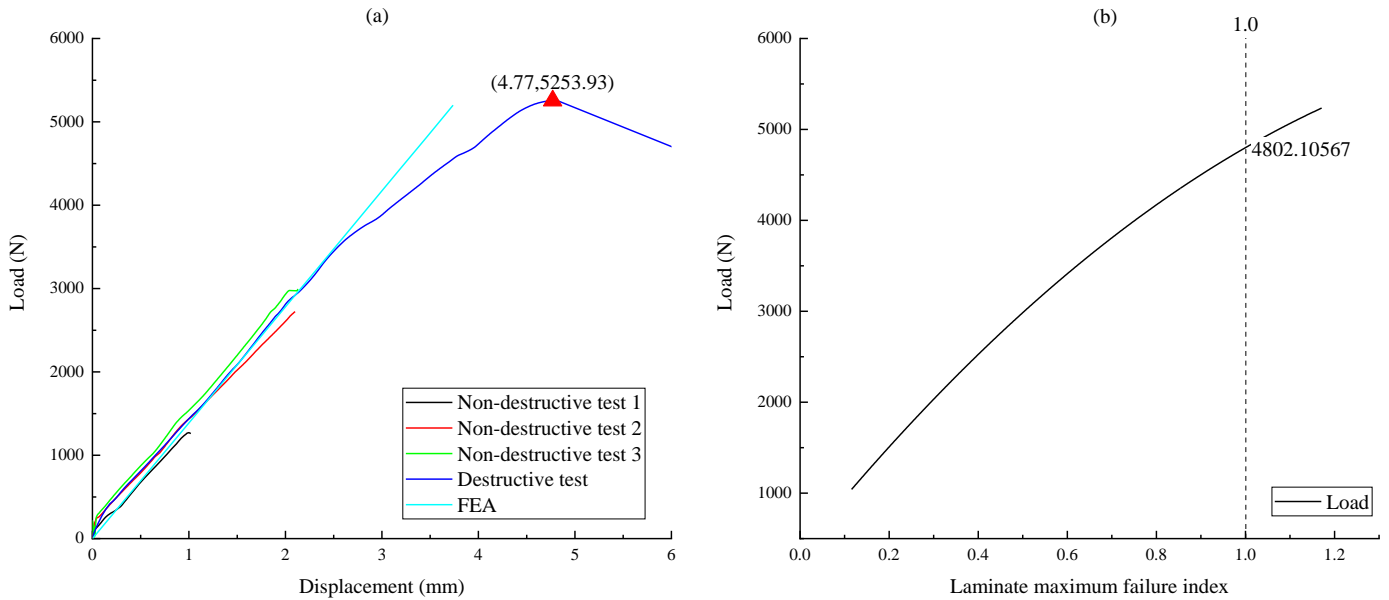


Figure 11 (a) Load-displacement results from experiment and FEA, (b) Laminate maximum failure index

The simulation then was performed for the same braided component but with different braid angles ( $20^\circ$ ,  $25^\circ$ ,  $30^\circ$  and  $35^\circ$ ) and different fibre volume fractions (40% and 50%). The FEA results for bending stiffness and strength of braided components are given in [Table 4](#). The increased fibre volume fractions can improve the bending stiffness of the braided tubular structure at the same braid angle. The percentage of the increase in stiffness was about the same as the increase in fibre content (25%). At the same braid angle, increased fibre volume fraction had an adverse effect on the bending strength of the tubular braided component, and this effect was minimum at *the braid angle of  $25^\circ$* . Both bending stiffness and strength of the braided component significantly decreased with increased braid angle.

Table 4 Stiffness and failure load results for braided components with various fibre angles and fibre volume fractions

Braid angle (degree)		Stiffness (N/mm)				Failure load (N)			
		20	25	30	35	20	25	30	35
FVF	40%	1629.8	1393	1086.6	799.5	5448.9	4751.3	3907.0	3222.1
	50%	2036.0	1742.7	1361.8	999.0	5275.0	4600.4	3752.3	3076.1
Difference		24.92%	25.10%	25.33%	24.95%	-3.19%	-3.17%	-3.96%	-4.53%

The selection of braid angles requires careful considerations on the expected mechanical properties of the components in a real application. Larger braid angle can be used if high flexibility is required but a high fibre volume fraction (50% or above) is favoured in all applications due to the fact that 1) the decrease in strength in axial direction resulted from increased fibre volume fraction is relatively small when compared to the benefit of increased stiffness; and 2) low fibre volume fraction could promote the occurrence of resin-rich regions within the composite.

## 4. Microscope observations

### 4.1 Fatigue and failure mode analysis

Based on *the* results from testing, the coupons were divided into three groups for observations, i.e. 1) coupons that have been through fatigue testing but have not yet reached critical failure conditions (still within second fatigue stage); 2) coupons that failed during the bending fatigue; and 3) coupons that failed in quasi-static bending tests. The observations were performed on upper surface, lower surface and side surface at the middle along the length of the specimens using the Leica S6 D Greenough stereo microscope. The further observation using JEOL JSM-6060LV SEM was focused on side surfaces. *A 25 mm × 25 mm section was cut from each damaged specimen using pneumatic tools and the side surface was left untouched for damage observation. Compressed air was used to remove the debris before observation.* The damages developed in three groups of test specimens are presented in Figure 12.

During the second fatigue stage, the developed damages are mainly located at the sites of stress concentration such as the voids/bubbles in the matrix, matrix pockets (the tip of where the warp and weft of fibre yarns meet) as shown in Figure 12 (a). There was small debonding of matrix and fibre yarn at matrix pockets along the centreline. On the lower surface, there were only debonding at the edge instead of the matrix pockets (Figure 12 (b)). However, there were discrete inter-yarn cracks developed in the bottom layer yarns (tension side) as shown in the side surface (Figure 12 (c)). These cracks formed in horizontal direction and turned towards the lower surface following the shape of the fibre yarns. The crack could not propagate any further in vertical direction into the fibre yarn and turned away to the boundary between two yarns. The size of the crack kept reducing as it propagated within the inter-yarn matrix. *These damages correspond to the low level of energy absorption per cycle as discussed in the previous section.*

At the third stage of fatigue, the damage initiated from the previous stage started growing rapidly. The size of the debonding area at the matrix pockets increased and *the* cracks started forming in the matrix at these areas on the upper surface as shown in Figure 12 (d). The buckling of the fibre yarn also formed at this stage on the upper surface (compression) and some of the buckling developed into failure as the breakage of fibre yarns. These very short broken fibres from kink band were spread around the major cracks. The debonding of fibre yarn and matrix also started forming at matrix pockets on the lower surface during this stage (Figure 12 (e)). The size of the inter-yarn cracks in the lower half (tension) of the side surface became larger and the cracks grew into adjacent ones to *form a long inter-yarn crack.* *These damages are the results of a higher level of hysteresis energy absorbed by the material.*

The modes of quasi-static bending failure were very similar to those of bending fatigue failure but with more serious effects. As shown in Figure 12 (f), the fibre kink bands can be found on the upper surface including an increased amount of severe fibre yarn breakages as a result of this buckling process. The cracks formed at different locations were developed into each other, forming a larger and wider crack along the width direction of the upper surface. There were short matrix cracks formed at the matrix pockets on the lower surface. On the side surface, there were cracks developed within some fibre yarns, leading to the disintegration of the fibre yarn into small fibre bundles. Although these intra-yarn cracks were overall inclined at a certain angle, they presented a more instable growth as there were more diversions along the routes compared with inter-yarn cracks. Individual fibres and small fibre bundles were split from the fibre yarns into the inter-yarn cracks (Figure 12 (i)).

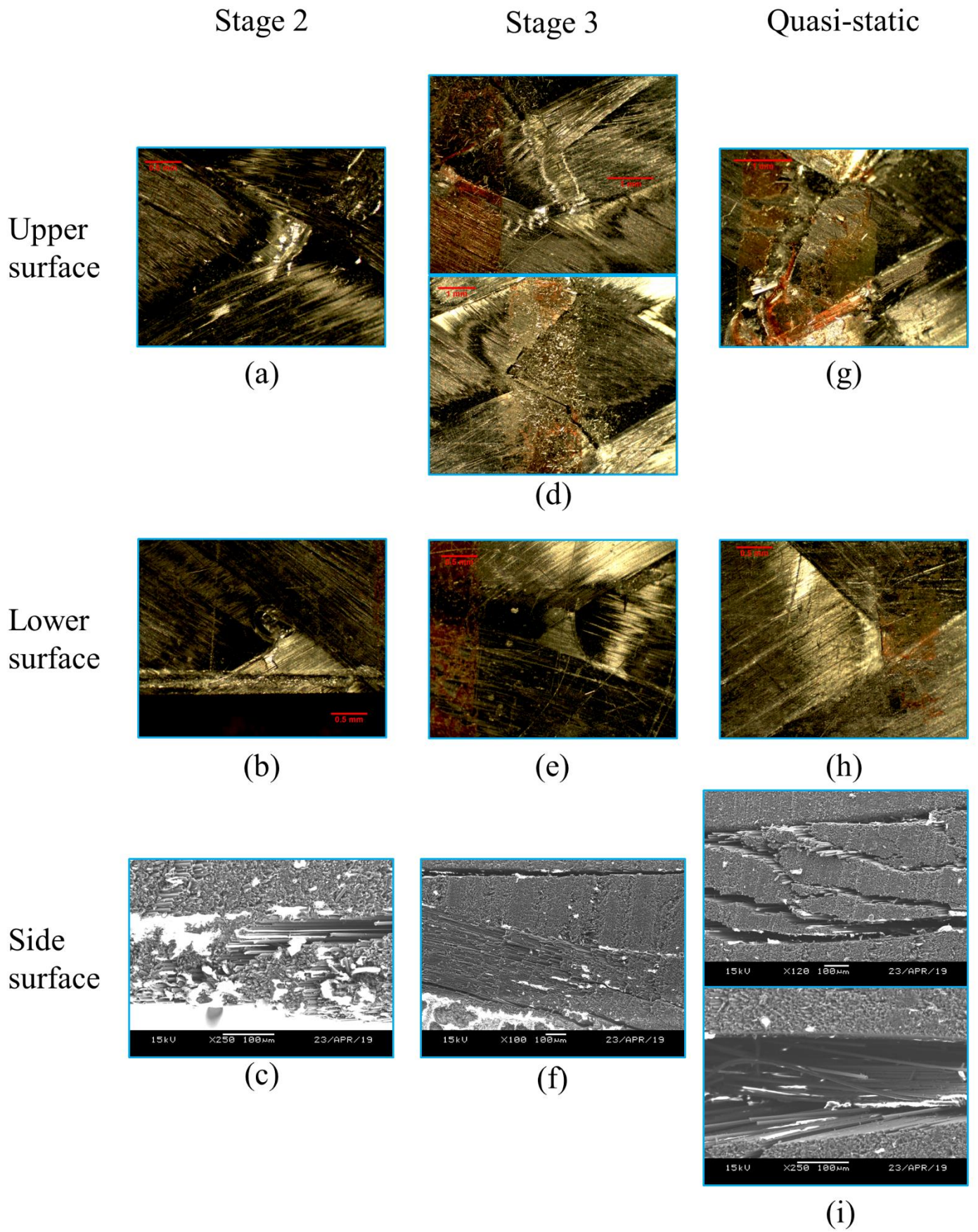


Figure 12 Damages on specimens from fatigue stage 2, stage 3 and quasi-static test

## 4.2 Process-induced defects

Figure 13 shows the voids in cured resin on the outer surface of the test specimen. The part of the fibre yarns within these cavities have a thinner layer of resin or no resin covered. The fibre-matrix interface at the edge of the voids is subject to higher stress when the samples are loaded, leading to early debonding and matrix cracks *as highlighted in Figure 13 (b)*.

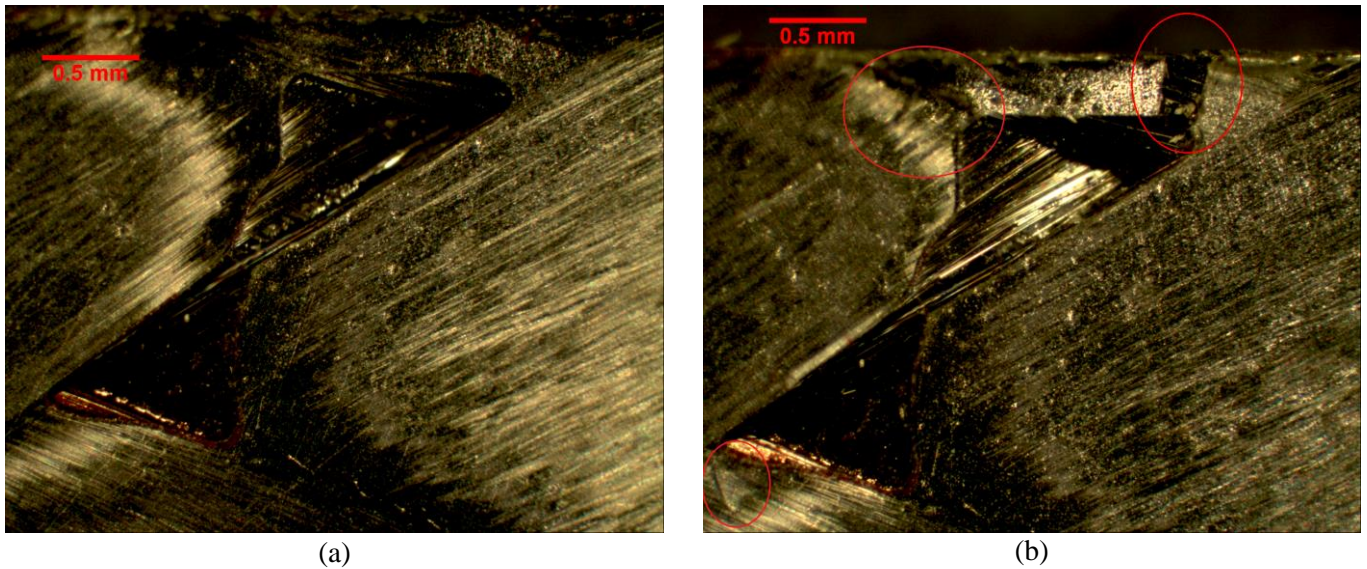


Figure 13 Matrix voids on the outer surface (a) before testing and (b) after testing

The presence of voids is the most significant defect in resin transfer moulded (RTM) composite materials and can *severely influence the mechanical properties. Mechanical performance of composites could be altered both locally and globally with voids acting as hot spots for stress concentrations. In current VARTM process, the void may form in composites due to the entrapment of air, initial air bubbles in the resin, evaporation of released agent and the volatilisation of dissolved gases or moisture in the resin during infusion and curing process. It was found from previous observations results that the matrix pockets are the sites where matrix voids predominantly occurred in braided composite manufactured from the current liquid moulding process. Various techniques need to be adopted to reduce the void content such as bleeding (keeping resin flowing well after the mould is filled), packing (keeping infusion after closing the resin exits) or applying additional compression to the mould cavity after the infusion is finished.*

*Figure 14 shows the severe matrix cracks at a locally resin-rich region as highlighted. The high reflection in the image was caused by the high amount of resin distribution in this region. Premature damages and cracks tend to occur at resin-rich area due to the lack of load-bearing reinforcement. The resin pocket is a minor resin-rich region hence the debonding always occurred at an early stage on the resin pockets as observed from the outer surface of specimens.*

These cavities between fibre yarns are an inherent defect for braided composites due to its relatively large fibre yarns and undulation. The size of the resin pockets and yarn waviness could be reduced if the material is tightly stacked during impregnation using higher pressure RTM. *The diverse results of flexural strength and modulus found between specimens with close FVF can be largely attributed to the void content and local resin-rich defects discussed above.*

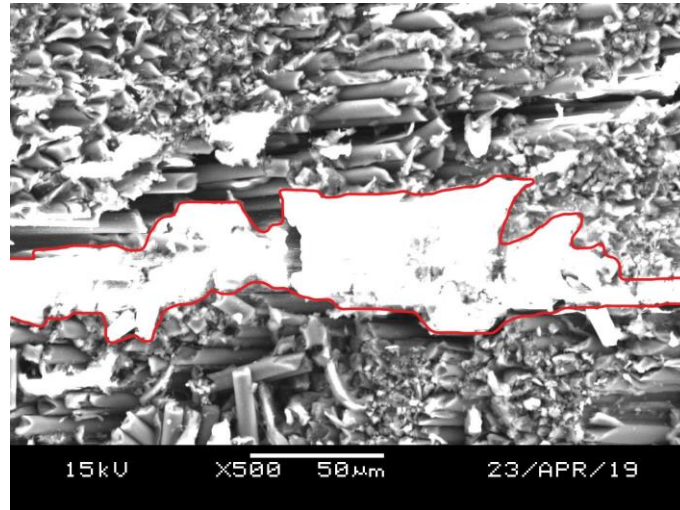


Figure 14 Resin-rich area and matrix cracks

As highlighted in Figure 15, there were fibres with ends covered with no resin at the undamaged area. These debonded fibre ends are lined up at an angle and each array is parallel to each other. This defect was specifically induced by cutting and trimming process for producing these samples. These debonded fibre ends would become susceptible to crack initiation when the composite is stressed and lead to intra-yarn cracks at a later stage. However, the braided composites are commonly used on tubular parts such as bike frames, pipes, etc, and the braid will not be cut open in most of the applications. *Flattened closed braid sleeves are recommended as preform for flat parts or panels to make use of increased material strength while avoiding the cutting induced defects.*

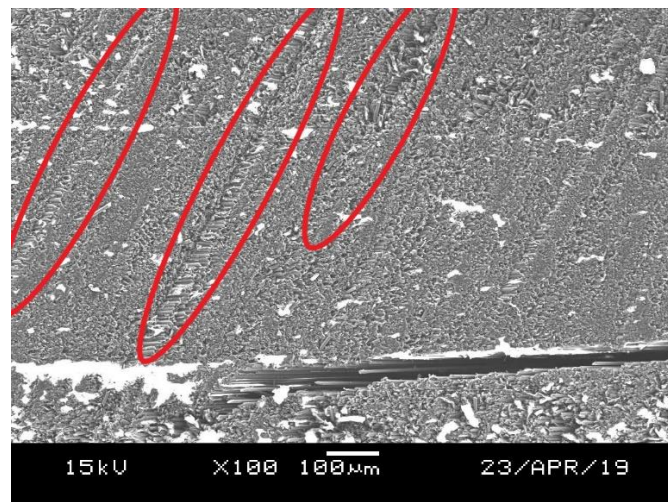


Figure 15 Debonding between fibre ends and matrix caused by trimming

## 5. Conclusions

In this work, experimental tests were performed for a  $\pm 25^\circ$  biaxial braided carbon fibre reinforced polymer (CFRP), which was manufactured using vacuum assisted resin transfer moulding (VARTM), subjected to quasi-static three-point bending and three-point bending fatigue loads. A finite element (FE) model was also developed, and the simulation results were compared against experimental data. The following conclusions can be drawn from the present study:

- 1) The flexural properties of this braided CFRP are seriously affected by the local fibre volume fractions, which is mostly determined by the manufacturing process. Specimens with greater fibre volume fractions tend to have higher flexural modulus but slightly lower flexural strength.
- 2) The flexural stiffness of the braided CFRP presents a strong hysteresis under loading and reloading in fatigue tests. There are three phenomenal stages for the decrease of the flexural modulus during the bending fatigue.
- 3) The failure process of braided CFRP is the continuous accumulation of micro or local damages. The major damage modes for fatigue are debonding of matrix and fibres at yarn edges (inter-yarn cracks) in both tension and compression *sides* of the specimen. Fibre yarn breakage caused by fibre buckling and matrix cracks were in the compression side.
- 4) The main process defects presented in test specimens are inter-yarn matrix voids, resin-rich regions and matrix-fibre ends debonding at the cut surface. The braid angle selection needs to consider expected mechanical performance of the braided structure.
- 5) The FE method adopted in this study combined with Tsai-Wu failure criterion has produced very close failure prediction at the component level. However, the FEA tends to over-predict the stress level for test specimens.

## Data availability

The raw/processed data required to reproduce these findings cannot be shared at this time as the data also forms part of an ongoing study.

## References

- [1] P. de Hanna, Development of a composites trailing arm for a helicopter main landing gear, in: Proc. Int. Symp. Compos. Manuf. Aircr. Struct., Marknesse, The Netherlands, 2010.
- [2] A. Erber, K. Birkefeld, K. Drechsler, The influence of braiding configuration on damage tolerance of drive shafts, in: SEICO 09, SAMEPE Eur. 30th Int. Jubil. Conf. Forum, Paris, France, 2009.
- [3] N. Dölle, FVK-anwendungen bei Daimler - lessons learned, in: CCeV Automot. Forum, Neckarsulm, 2010.

- [4] O. Rüger, *Preforming: Stand der Techni & Ausblick*, (2009). <https://www.carbon-composites.eu/> (accessed February 15, 2019).
- [5] B. Arold, A. Gessler, C. Metzner, K. Birkefeld, Braiding processes for composites manufacture, in: *Adv. Compos. Manuf. Process Des.*, Elsevier, 2015: pp. 3–26. <https://doi.org/10.1016/B978-1-78242-307-2.00001-4>.
- [6] J. Cichosz, T. Wehrkamp-Richter, H. Koerber, R. Hinterhölzl, P.P. Camanho, Failure and damage characterization of ( $\pm 30^\circ$ ) biaxial braided composites under multiaxial stress states, *Compos. Part A Appl. Sci. Manuf.* 90 (2016) 748–759. <https://doi.org/10.1016/j.compositesa.2016.08.002>.
- [7] M. Yekani Fard, B. Raji, J. Woodward, M. Padilla, Experimental characterization of damage mechanisms of seamless net-shaped circular pre-form and overlapped stitched composite pipes, *Polym. Test.* 78 (2019) 105934. <https://doi.org/10.1016/j.polymertesting.2019.105934>.
- [8] A.G. Evans, W.F. Adler, Kinking as a mode of structural degradation in carbon fiber composites, *Acta Metall.* 26 (1978) 725–738. [https://doi.org/10.1016/0001-6160\(78\)90023-8](https://doi.org/10.1016/0001-6160(78)90023-8).
- [9] J.M. Hedgepeth, P. Van Dyke, Local Stress Concentrations in Imperfect Filamentary Composite Materials, *J. Compos. Mater.* 1 (1967) 294–309. <https://doi.org/10.1177/002199836700100305>.
- [10] B. Rosen, *Mechanics of composite strengthening: fibre composites*, American Society of Metals, 1965.
- [11] B. Budiansky, N.A. Fleck, Compressive failure of fibre composites, *J. Mech. Phys. Solids.* 41 (1993) 183–211. [https://doi.org/10.1016/0022-5096\(93\)90068-Q](https://doi.org/10.1016/0022-5096(93)90068-Q).
- [12] R. Cai, T. Jin, The effect of microstructure of unidirectional fibre-reinforced composites on mechanical properties under transverse loading: A review, *J. Reinf. Plast. Compos.* 37 (2018) 1360–1377. <https://doi.org/10.1177/0731684418796308>.
- [13] D. Grund, M. Orlishausen, I. Taha, Determination of fiber volume fraction of carbon fiber-reinforced polymer using thermogravimetric methods, *Polym. Test.* 75 (2019) 358–366. <https://doi.org/10.1016/j.polymertesting.2019.02.031>.
- [14] K.H.G. Ashbee, Bi-Dimensional Compression Moulding of Super-High Fibre Volume Fraction Composites, *J. Compos. Mater.* 20 (1986) 114–124. <https://doi.org/10.1177/002199838602000201>.
- [15] C. McCarthy, T. Vaughan, Micromechanical failure analysis of advanced composite materials, in: *Numer. Model. Fail. Adv. Compos. Mater.*, Elsevier, 2015: pp. 379–409. <https://doi.org/10.1016/B978-0-08-100332-9.00014-1>.
- [16] G. Qi, B. Zhang, Y. Yu, Research on carbon fiber/epoxy interfacial bonding characterization of transverse fiber bundle composites fabricated by different preparation processes: Effect of fiber volume fraction, *Polym. Test.* 52 (2016) 150–156. <https://doi.org/10.1016/j.polymertesting.2016.03.022>.
- [17] E.M. Jensen, *Creep and Creep Rupture of Fibre Reinforced Polymers: Long Term Variability*, University of Wyoming, 2014. <http://adsabs.harvard.edu/abs/2014PhDT.....71J>.
- [18] G.W. Melenka, J.P. Carey, Braid CAM: Braided composite analytical model, *SoftwareX.* 7 (2018) 23–27. <https://doi.org/10.1016/j.softx.2017.12.004>.

- [19] C. Zhao, Y. Huang, Z. Chen, S.K. Ha, Progressive failure prediction of a landing gear structure of braided composites, *Compos. Struct.* 161 (2017) 407–418. <https://doi.org/10.1016/j.compstruct.2016.11.076>.
- [20] A.D. Kelkar, J.D. Whitcomb, *Characterisation and structural behaviour of braided composites*, Washington, DC, 2009. <https://doi.org/DOT/FAA/AR-08/52>.
- [21] A. Aggarwal, S. Ramakrishna, V.K. Ganesh, Predicting the Strength of Diamond Braided Composites, *J. Compos. Mater.* 36 (2002) 625–643. <https://doi.org/10.1177/0021998302036005487>.
- [22] A.K. Pickett, M.R.C. Fouinneteau, Material characterisation and calibration of a meso-mechanical damage model for braid reinforced composites, *Compos. Part A Appl. Sci. Manuf.* 37 (2006) 368–377. <https://doi.org/10.1016/j.compositesa.2005.03.034>.
- [23] J. TATE, A. KELKAR, J. WHITCOMB, Effect of braid angle on fatigue performance of biaxial braided composites, *Int. J. Fatigue.* 28 (2006) 1239–1247. <https://doi.org/10.1016/j.ijfatigue.2006.02.009>.
- [24] J.S. Tate, A.D. Kelkar, Stiffness degradation model for biaxial braided composites under fatigue loading, *Compos. Part B Eng.* 39 (2008) 548–555. <https://doi.org/10.1016/j.compositesb.2007.03.001>.
- [25] L. Wu, F. Zhang, B. Sun, B. Gu, Finite element analyses on three-point low-cyclic bending fatigue of 3-D braided composite materials at microstructure level, *Int. J. Mech. Sci.* 84 (2014) 41–53. <https://doi.org/10.1016/j.ijmecsci.2014.03.036>.
- [26] W. Hao, Y. Yuan, X. Yao, Y. Ma, Computational analysis of fatigue behavior of 3D 4-directional braided composites based on unit cell approach, *Adv. Eng. Softw.* 82 (2015) 38–52. <https://doi.org/10.1016/j.advengsoft.2014.12.007>.
- [27] E.M. Jensen, D.A. Leonhardt, R.S. Fertig, Effects of thickness and fiber volume fraction variations on strain field inhomogeneity, *Compos. Part A Appl. Sci. Manuf.* 69 (2015) 178–185. <https://doi.org/10.1016/j.compositesa.2014.11.019>.
- [28] M. Mühlstädt, W. Seifert, M.M.L. Arras, S. Maenz, K.D. Jandt, J. Bossert, 3D model of intra-yarn fiber volume fraction gradients of woven fabrics, *Compos. Struct.* 180 (2017) 944–954. <https://doi.org/10.1016/j.compstruct.2017.08.049>.
- [29] T. Wehrkamp-Richter, N. V. De Carvalho, S.T. Pinho, Predicting the non-linear mechanical response of triaxial braided composites, *Compos. Part A Appl. Sci. Manuf.* 114 (2018) 117–135. <https://doi.org/10.1016/j.compositesa.2018.08.011>.
- [30] J.C. Faes, A. Rezaei, W. Van Paepegem, J. Degrieck, Accuracy of 2D FE models for prediction of crack initiation in nested textile composites with inhomogeneous intra-yarn fiber volume fractions, *Compos. Struct.* 140 (2016) 11–20. <https://doi.org/10.1016/j.compstruct.2015.12.024>.
- [31] J. Tate, A. Kelkar, J. Rice, Feasibility study of VARTM manufacturing of carbon biaxial braided composites using EPON 9504 epoxy resin system, in: *JISSE-8, 8th Int. SAMPE Symp. Exhib.*, Tokyo, Japan, 2003.
- [32] K.-T. Hsiao, D. Heider, Vacuum assisted resin transfer molding (VARTM) in polymer matrix composites, in: *Manuf. Tech. Polym. Matrix Compos.*, Elsevier, 2012: pp. 310–347.

<https://doi.org/10.1533/9780857096258.3.310>.

- [33] S.G. ADVANI, E.M. SOZER, Liquid Molding of Thermoset Composites, in: *Compr. Compos. Mater.*, Elsevier, 2000: pp. 807–844. <https://doi.org/10.1016/B0-08-042993-9/00171-6>.
- [34] F. Heieck, F. Hermann, P. Middendorf, K. Schladitz, Influence of the cover factor of 2D biaxial and triaxial braided carbon composites on their in-plane mechanical properties, *Compos. Struct.* 163 (2017) 114–122. <https://doi.org/10.1016/j.compstruct.2016.12.025>.
- [35] Toray Composite Materials America Inc., T700G PRELIMINARY DATA SHEET, (n.d.). [https://www.toraycma.com/file\\_viewer.php?id=4458](https://www.toraycma.com/file_viewer.php?id=4458) (accessed February 17, 2019).
- [36] Scott Bader, Crestapol® 1260 Flyer UK, (n.d.). <https://www.scottbader.com/wp-content/uploads/Crestapol-1260-Flyer-UK.pdf> (accessed February 17, 2019).
- [37] ASTM D790, Standard Test Methods for Flexural Properties of Unreinforced and Reinforced Plastics and Electrical Insulating Materials, West Conshohocken, PA, 2017. <https://doi.org/10.1520/D0790-17>.
- [38] C. Zweben, W. Smith, M. Wardle, Test Methods for Fiber Tensile Strength, Composite Flexural Modulus, and Properties of Fabric-Reinforced Laminates, in: *Fifth Conf. Compos. Mater. Test. Des.*, ASTM International, 100 Barr Harbor Drive, PO Box C700, West Conshohocken, PA 19428-2959, n.d.: pp. 228-228–35. <https://doi.org/10.1520/STP36912S>.
- [39] R. Talreja, Fatigue of Polymer Matrix Composites, in: *Compr. Compos. Mater.*, Elsevier, 2000: pp. 529–552. <https://doi.org/10.1016/B0-08-042993-9/00070-X>.
- [40] J.W.M. Mens, A.W.J. de Gee, Friction and wear behaviour of 18 polymers in contact with steel in environments of air and water, *Wear.* 149 (1991) 255–268. [https://doi.org/10.1016/0043-1648\(91\)90378-8](https://doi.org/10.1016/0043-1648(91)90378-8).
- [41] S.W. Tsai, E.M. Wu, A General Theory of Strength for Anisotropic Materials, *J. Compos. Mater.* 5 (1971) 58–80. <https://doi.org/10.1177/002199837100500106>.